BIOCHEMISTRY
including biophysical chemistry & molecular biology

Article

pubs.acs.org/biochemistry

Physical Characterization of the Manganese-Sensing Pneumococcal Surface Antigen Repressor from *Streptococcus pneumoniae*

John P. Lisher,[†,‡] Khadine A. Higgins,[‡] Michael J. Maroney,[§] and David P. Giedroc*[,†,‡]

[†]Department of Chemistry and [‡]Interdisciplinary Graduate Program in Biochemistry, Indiana University, Bloomington, Indiana 47405-7102, United States

[§]Department of Chemistry, University of Massachusetts, Amherst, Massachusetts 01003, United States

Supporting Information

ABSTRACT: Transition metals, including manganese, are required for the proper virulence and persistence of many pathogenic bacteria. In *Streptococcus pneumoniae* (*Spn*), manganese homeostasis is controlled by a high-affinity Mn(II) uptake complex, PsaBCA, and a constitutively expressed efflux transporter, MntE. *psaBCA* expression is transcriptionally regulated by the DtxR/MntR family metalloregulatory protein pneumococcal surface antigen repressor (PsaR) in *Spn*. Here, we present a comprehensive analysis of the metal and DNA binding properties of PsaR. PsaR is a homodimer in the absence and presence of metals and binds two manganese or zinc atoms per protomer (four per dimer) in two pairs of structurally distinct sites, termed site 1 and site 2. Site 1 is likely filled with Zn(II) *in vivo* ($K_{Zn1} \geq 10^{13}$ M^{-1}; $K_{Mn1} \approx 10^{8}$ M^{-1}). The Zn(II)−site 1 complex adopts a pentacoordinate geometry as determined by X-ray absorption spectroscopy containing a single cysteine and appears to be analogous to the Cd(II) site observed in *Streptococcus gordonii* ScaR. Site 1 is necessary but not sufficient for full positive allosteric activation of DNA operator binding by metals as measured by ΔG_c, the allosteric coupling free energy, because site 1 mutants show an intermediate ΔG_c. Site 2 is the primary regulatory site and governs specificity for Mn(II) over Zn(II) in PsaR, where $\Delta G_c^{Zn,Mn} \gg \Delta G_c^{Zn,Zn}$ despite the fact that Zn(II) binds site 2 with an affinity 40-fold higher than that of Mn(II); i.e., $K_{Zn2} > K_{Mn2}$. Mutational studies reveal that Asp7 in site 2 is a critical ligand for Mn(II)-dependent allosteric activation of DNA binding. These findings are discussed in the context of other well-studied DtxR/MntR Mn(II)/Fe(II) metallorepressors.

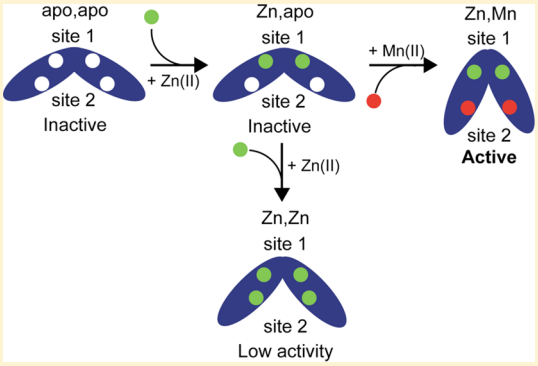

Transition metals constitute an array of critical micronutrients for nonpathogenic and pathogenic bacteria alike and provide required structural or catalytic functions tied to optimal growth or pathogenesis.[1,2] Although these metals are required under normal conditions, deprivation of these metals or an excess of these metals can severely impair bacterial growth. As a result, bioavailable metal concentrations are actively maintained inside the cell to allow for optimal growth under a wide range of prevailing conditions. This process, termed metal ion homeostasis, is orchestrated via coordinated transcriptional control of the expression of both metal uptake and efflux systems.[3,4]

Manganese has emerged as a biologically significant micronutrient as a result of the accumulation of evidence of its role in modulating the oxidative stress response inside cells.[5] Indeed, vertebrates employ a Ca^{2+}-activated Mn(II) and Zn(II) chelating protein, calprotectin, which provides broad-range inhibition of microbial growth via extracellular sequestration of Mn(II) and/or Zn(II), in an effort to deprive microorganisms of this essential metal(s).[6−9] In *Escherichia coli*, transcriptional activation of the oxidative stress sensor OxyR induces this iron-centric bacterium to import manganese and replace mononuclear Fe(II) in a number of enzymes with Mn(II); this protects these enzymes against H_2O_2 damage.[10−12] Manipulation of intracellular manganese concentrations has also been connected to protecting other bacteria from oxidative damage through both enzyme-mediated, e.g., via Mn(II) superoxide dismutase, and enzyme-independent means.[13−16] *Streptococcus pneumoniae* may well utilize similar mechanisms to combat both endogenous and exogenous oxidative stress encountered during infections.[17] We have previously shown that *S. pneumoniae* concentrates manganese to a whole cell-associated concentration approaching that of zinc and greater than that of iron despite a concentration of manganese that is ≈50-fold lower than that of either metal in the growth medium.[18] Additionally, it has been shown that extracellular zinc stress induces an ≈40% reduction in total cell-associated Mn(II) and a growth defect likely caused by competition at the Mn(II) uptake transporter protein PsaA; as a result, there is transcriptional upregulation of the PsaR regulon under these conditions. Addition of excess manganese restores both normal growth and manganese concentrations.[18,19] These data tie bioavailable manganese

Received: August 18, 2013
Revised: September 17, 2013
Published: September 25, 2013

   dx.doi.org/10.1021/bi401132w | *Biochemistry* 2013, 52, 7689−7701

directly to the viability of *S. pneumoniae*, leading us to further explore how manganese levels are regulated in the cell.

Members of the MntR/DtxR repressor family are primarily responsible for mediating transcriptional control of iron or manganese uptake.[20,21] The three most extensively studied members of this family are the homologous Fe(II) sensors *Corynebacterium diphtheriae* DtxR and *Mycobacterium tuberculosis* IdeR[22,23] and the Mn(II) sensor in *Bacillus subtilis*, MntR.[24−31] Although similar in both the primary structure and the quaternary structure of the activated metal-bound forms (see Figure S1 of the Supporting Information), DtxR and MntR induce transcriptional corepression by binding their cognate metal ions in distinct ways. DtxR requires binding to a pair of ancillary sites near the C-terminal SH3-like domain to induce protein dimerization; further binding to a pair of regulatory sites allosterically activates DNA binding and promotes transcriptional repression.[22,23] *B. subtilis* MntR also requires the binding of four metal ions for activation of DNA binding but lacks the C-terminal SH3-like domain of DtxR and instead employs a binuclear Mn(II) cluster to activate DNA binding.[32] The precise coordination structure of the binuclear cluster observed in crystallographic studies is dependent on temperature, giving rise to so-called A/B (observed only at 100 °C) and A/C Mn(II) clusters. The A/C cluster conformation is thought to be the physiologically relevant one, in which the Mn(II) ions are separated by 4.4 Å; the A/C conformer is also most consistent with the electron paramagnetic resonance (EPR) studies in solution that show a spin-coupling interaction consistent with a longer (>4 Å) distance between the two Mn(II) ions.[28] Both Mn(II) ions must be bound to fully activate DNA binding, with the A site thought to function as a "Mn(II) selectivity filter" that favors occupancy of the C site with cognate Mn(II). Binding of noncognate Zn(II), Co(II), and Fe(II), for example, fills only the A site, and none strongly activate DNA binding.[33] Recent experiments reveal that the A site Mn(II) ion in the A/C cluster can be replaced by a positively charged Lys ε-NH_2 chain via mutagenesis (E11K) in MntR with retention of full biological activity.[33]

These differences between DtxR and MntR suggest that this common core DtxR/MntR family scaffold may have evolved unique mechanisms of allosteric activation of DNA operator binding in related repressors in other bacteria, as well.[33] Consistent with this, the crystallographic structure of the dimeric Mn(II)-sensing repressor ScaR from *Streptococcus gordonii*[34] determined to ≈2.7 Å resolution reveals either a Zn(II) or Cd(II) ion bound to a site positioned between the dimerization and FeoA domains that is distinct from that previously found for the ancillary sites in DtxR.[34] The N-terminal winged helical DNA-binding domains in each protomer in this highly asymmetric dimer are splayed out relative to one another. This suggests that the primary activating site is not filled in this structure and, as a result, likely corresponds to the inactive DNA-binding state. Metal binding studies showed between two and three Mn(II) ions may bind per protomer.[34] The overall conclusion from this work is that ScaR and related Mn(II)-regulated repressors from other streptococci are superficially similar to DtxR and are capable of binding Mn(II), which, in turn, activates DNA operator−promoter binding. The structural mechanism, however, remains incompletely understood.

In this work, we use the various crystallographic structures of *B. subtilis* MntR[24,25,32,33] and the Cd(II)-bound *S. gordonii* (*Sgo*) ScaR structure[34] as well as our previous findings[18] as a guide to elucidate the metal binding properties of *Spn* PsaR in solution. PsaR is 76% identical in sequence to *Sgo* ScaR. We present new insights into the mechanism of allosteric activation of *psaBCA* operator (PsaO) binding by PsaR induced by Mn(II) versus Zn(II). We show that PsaR is a stable homodimer in all metallation states and harbors two pairs of transition metal sites (four per dimer) denoted sites 1 and 2. Metal binding studies show that site 1 is likely filled with Zn(II) *in vivo* with a K_{Zn}^{1} of $\geq 10^{13}$ M^{-1}; site 1 is required for full allosteric activation and may function more as a structural site that dampens the conformational heterogeneity of the *Spn* PsaR homodimer. X-ray absorption spectroscopy reveals that this metal site is analogous to the Cd(II) site observed in the *Sgo* ScaR structure.[34] The metal selectivity and DNA activation of *Spn* PsaR are dictated solely by site 2. Although site 2 binds noncognate metal Zn(II) with an ≈40-fold higher affinity than Mn(II) (pH 8.0 and 0.2 M NaCl), Mn(II) bound to site 2 to form $PsaR^{Zn,Mn}$ is characterized by an allosteric coupling free energy, ΔG_c, that is greater than twice that of Zn(II) bound to site 2 to form $PsaR^{Zn,Zn}$, thus making PsaR a Mn(II)-specific repressor. Mutational studies of sites 1 and 2 reveal that Asp7 in site 2 is a critical ligand for Mn(II)-dependent allosteric activation of DNA binding, a finding consistent with the analogous residue in this position functioning as a key driver of the Mn(II)-induced conformational switching in MntR[24] and as an important metal specificity determinant [Mn(II) vs Fe(II)] in *B. subtilis* MntR.[25]

MATERIALS AND METHODS

Chemicals and Reagents. All water used in these experiments was Milli-Q deionized (>18 MΩ), and the buffers were obtained from Sigma. Indicator dyes mag-fura-2 (mf2) and quin-2 were obtained from Invitrogen and Sigma, respectively. Metal stocks were made with Ultra Pure Alfa Aesar metals. All other reagents were as indicated in the text. An Ätka 10 purifier (GE) was used for all chromatographic separations. All metal binding and DNA binding experiments were performed under aerobic conditions as described below.

Subcloning and Introduction of Missense Mutations into the *psaR* Gene. The *psaR* gene (locus tag SPD_1450) was amplified from *S. pneumoniae* D39 genomic DNA using cloning primers containing *Nde*I and *Bam*HI restriction sites. The *psaR* insert was subcloned into expression vector pET3a restricted with *Nde*I and *Bam*HI to create pET-PsaR containing the wild-type *psaR* gene under transcriptional control of the T7 promoter. PsaR mutants were generated using the protocol supplied by QuikChange (Stratagene) using pET-PsaR as the template and an appropriate mutagenic primer. The integrity of all expression plasmids was verified by double-stranded dideoxy sequencing. The plasmids were transformed into Rosetta BL21(DE3) pLysS cells for protein expression.

Expression and Purification of Wild-Type and Mutant PsaRs. Competent cells were transformed with the desired pET-PsaR plasmid, plated onto an a plate with ampicillin and chloramphenicol (100 and 37 μg/mL, respectively), and grown overnight at 37 °C. Single colonies were used to inoculate 100 mL LB cultures containing both ampicillin and chloramphenicol and were grown overnight at 37 °C while being shaken. The overnight cultures were diluted into 1 L of LB and grown at 37 °C while being shaken. Overexpression of PsaR was accomplished by induction of 1 L of midlog LB cultures with IPTG (Inalco) to a final concentration of 0.4 mM for 2.5 h at 37 °C. The cells were harvested and resuspended in 25 mM

MES (pH 6.0), 750 mM NaCl, 2 mM DTT, and 5 mM EDTA. The resuspended cells were lysed by sonication and centrifuged at 6750*g* for 20 min. A 10% polyethyleneimine (PEI) solution was added to the supernatant to a final concentration of 0.15% (v/v) and allowed to mix for 30 min at 4 °C to precipitate nucleic acids. The precipitate was removed by centrifugation for 20 min. Finally, a two-step ammonium sulfate precipitation protocol was used to precipitate PsaR from PEI and other contaminating proteins. The final 50% ammonium sulfate pellet was obtained by centrifugation for 15 min and resuspended in buffer M [25 mM MES (pH 6.0), 2 mM DTT, and 5 mM EDTA]. The resuspended sample was dialyzed extensively into buffer M containing 100 mM NaCl, with the supernatant loaded onto a cation exchange resin (SP-Sepharose, flow rate of 2 mL/min, NaCl gradient from 0.1 to 0.75 M over 90 min). PsaR-containing fractions were assessed using sodium dodecyl sulfate−polyacrylamide gel electrophoresis, pooled, concentrated using Centrifugal filter units (Millipore), and applied to a size exclusion column (Superdex 200 16/60 prep grade). All PsaRs migrated with an elution time consistent with that of a dimer. The PsaR-containing fractions were collected and dialyzed into 50 mM Tris (pH 8.0), 200 mM NaCl, and 2 mM TCEP (with 10 g/L Chelex 100 resin), filtered, aliquoted into small aliquots, and stored at −80 °C for further use. Wild-type and mutant PsaRs were subjected to electrospray ionization mass spectrometry to confirm the expected mass. Protein concentrations were calculated using a predicted extinction coefficient of 11920 M^{-1} cm^{-1} at 280 nm (ProtParam).

Metal Binding Stoichiometry and Affinity Determinations. Purified Apo-PsaR was diluted into chelexed metal binding buffer [50 mM Tris (pH 8.0) and 100 mM NaCl]. A fixed concentration of metal-free mag-fura-2 (mf2) or quin-2 was added to the solution, yielding a final volume of 1 mL. Metal stocks of Mn(II) or Zn(II) in the same buffer were titrated into the protein/competitor solution and the spectra from 250 to 600 nm taken following a 2 min incubation. For mf2 experiments, the absorbance at 360 and 325 nm was monitored; those values report on the λ_{max} for the metal-free and metal-bound states of mf2, respectively. For quin-2 experiments, the decrease in absorbance at 265 nm was monitored following a 20 min incubation after each addition. All metal binding experiments were conducted with a Hewlett-Packard model 8452A spectrophotometer at room temperature. The mf2 binding curves were fit to an appropriate two-step or one-step competition binding model with a K_{Zn}^{mf2} of 5.0×10^7 M^{-1} [35] or a K_{Mn}^{mf2} of 2.4×10^6 M^{-1} determined by direct titration (see Figure S2 of the Supporting Information). Quin-2 binding curves were fit to a one-step binding model with a K_{Zn}^{quin2} of 2.7×10^{11} M^{-1}.[36] A Ω value of 5 was used to account for the Tris-Zn(II) competition under these solution conditions;[37] no correction was necessary for the Tris-Mn(II) competition (Ω ≈ 1).[38] All binding curves were determined in triplicate and globally fit to a simple competition model using Dynafit (see Figure S3 of the Supporting Information for a sample Dynafit script file).[39]

DNA Binding Assays. A MerMade 4 instrument was used to synthesize complementary oligonucleotides corresponding to the *psaBCA* operator−promoter region (5′-TTCAAAAAT-TAACTTGACTTAATTTTTTTT-Flu-3′ and 5′-AAAAAAAA-TTAAGTCAAGTTAATTTTTGA-3′, where Flu is fluorescein). The crude oligonucleotides were cleaved from the column using AMA (1:1 methylamine/ammonium hydroxide mixture), precipitated with ethanol, dried overnight, and resuspended in 750 μL of 50 mM potassium phosphate (pH 6.0) and 7 M urea. Purified oligonucleotides were obtained using a ResQ column (flow rate of 1 mL/min, 0 to 1 M NaCl over 60 min). The concentration of the primers was determined by their predicted extinction coefficients of 308300 and 286500 M^{-1} cm^{-1} for the fluorescein-labeled and unlabeled strands, respectively. The single-stranded DNAs were annealed with a slight excess of unlabeled primer in the presence of a high salt concentration (500 mM NaCl), heated at 65 °C for 10 min, and allowed to cool in the dark for several hours for optimal annealing to obtain PsaO DNA. Aliquots of the annealed PsaO duplex were diluted to approximately 1.5 μM and used as is.

Fluorescence anisotropy measurements were performed by using a Biotek Synergy H1 Hybrid Multimode microplate reader with a λ_{ex} of 487 nm. A typical experiment was conducted in triplicate in a 96-well format with 10 nM duplex DNA operator in 50 mM Tris, 200 mM NaCl, and 2 mM TCEP (pH 8.0) at 25.0 °C unless noted otherwise, and various concentrations of PsaR. Metalated PsaRs were prepared by adding 0.95 molar protomer equivalent of Zn(II) followed by no addition ($PsaR^{Zn,apo}$) or 1.05 molar equivalents of the desired divalent metal, e.g., Mn(II) to create $PsaR^{Zn,Mn}$ or Zn(II) to create $PsaR^{Zn,Zn}$. To ensure full occupancy of the second metal site when desired, an additional 10 μM of the indicated divalent metal was added to the anisotropy buffer. The resulting data were fit to a dissociable dimer binding model that invokes the dimerization of PsaR (K_{dimer}), followed by binding of the dimer to the DNA (K_{DNA}) using Dynafit.[39] K_{dimer} was fixed to a value of 2.0×10^6 M^{-1} as estimated by an unconstrained fit to a titration of $PsaR^{Zn,Mn}$ to DNA.[18] Using this model with K_{dimer} constrained to this value for all PsaRs, the association constant, K_{DNA}, was determined (see Figure S4 of the Supporting Information for a sample Dynafit script file). The Gibbs allosteric coupling free energy (ΔG_c) of interest is operationally defined with the equation $\Delta G_c = -RT \ln(K_{DNA}^{Zn,Mn}/K_{DNA}^{Zn,apo})$. The errors associated with this value were determined as previously described.[40]

Multiangle Light Scattering Measurements. Wild-type PsaRs with different metallation states were prepared by dialyzing apo-PsaR into a MALS buffer [20 mM HEPES (pH 7.0), 200 mM NaCl, and 1 mM TCEP], followed by addition of nothing ($PsaR^{apo,apo}$), 0.95 molar protomer equivalent of Zn(II) ($PsaR^{Zn,apo}$), followed by 1.05 molar equivalents of Zn(II) ($PsaR^{Zn,Zn}$) or Mn(II) ($PsaR^{Zn,Mn}$). MALS measurements were performed on a Wyatt Technology DAWN HELEOS II multiangle light scattering (MALS) instrument coupled to a Wyatt Technology Optilab rEx refractive index (RI) detector; 100 μL of each sample (ranging from 150 to 160 μM protomer) was loaded onto a pre-equilibrated Superdex G75 10/300GL (GE) size exclusion column at a flow rate of 0.5 mL/min. SEC-MALS data were analyzed using Wyatt Technology ASTRA software to obtain the molar mass.

X-ray Absorption Spectroscopy (XAS). Wild-type $PsaR^{Zn,apo}$ or $PsaR^{Zn,Mn}$ was prepared by addition of 0.98 molar protomer equivalent of $Zn(CH_3COO)_2 \cdot 2H_2O$, followed by no addition, or addition of 1.05 molar equivalents of $MnSO_4$, respectively, in 50 mM Tris (pH 8.0), 200 mM NaBr, and 1 mM TCEP; 620 μM $PSA^{Zn,apo}$ and 560 μM $PsaR^{Zn,Mn}$ samples were prepared by syringe injection into polycarbonate XAS holders wrapped in kapton tape and frozen rapidly in liquid nitrogen. XAS data were collected as previously

dx.doi.org/10.1021/bi401132w | *Biochemistry* 2013, 52, 7689−7701

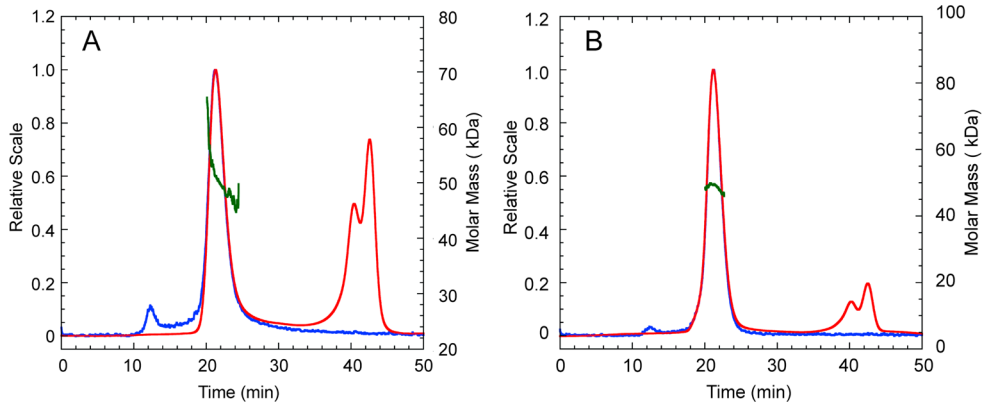

Figure 1. Representative multiangle light scattering (MALS) traces of wild-type PsaR^{apo,apo} (A) and PsaR^{Zn,apo} (B). The red trace shows the refractive index; the blue trace shows the Raleigh ratio. The red peak at ≈40 min in each panel marks the included volume of the column and is not protein. The green trace shows the determined molar mass (kilodaltons) across the main eluting species. Parameters for all metalated derivatives are listed in Table 1.

described[41] under dedicated ring conditions on beamline X3b at the National Synchrotron Light Source (NSLS), Brookhaven National Laboratories (Upton, NY). The samples were loaded into an aluminum sample holder, which was cooled to ∼50 K by using a He displex cryostat. Data were collected under ring conditions of 2.8 GeV and 120−300 mA using a sagitally focusing Si(111) double-crystal monochromator. Harmonic rejection was accomplished with a Ni-coated focusing mirror. X-ray fluorescence was collected using a 30-element fluorescence detector (Canberra). XANES were collected from 200 to −200 eV relative to the metal edge. The X-ray energy for the Zn K_α-edge was internally calibrated to the first inflection point of the corresponding metal foil, Zn, 9660.7 eV. EXAFS was collected to 13.5−16 k above the edge energy (E_o), depending on the signal:noise ratio at high values of k.

Data Reduction and Analysis. The XAS data reported are the average of six to eight scans. XANES and EXAFS data were analyzed using EXAFS123[42] and SixPack,[43] respectively. The SixPack fitting software builds on the ifeffit engine.[44,45] For the EXAFS analysis, each data set was background-corrected and normalized. The data were converted to k -space using the relationship

$$k = [2m_e(E - E_o)/\hbar^2]^{1/2}$$

where m_e is the mass of the electron, $\hbar$ is Plank's constant divided by 2π, and E_o is the threshold energy of the absorption edge. The threshold energy chosen for Zn was 9670 eV.[41] A Fourier transform of the data was produced using the k data range of 2−12.5 Å^{-1}, where the upper limit was determined by the signal:noise ratio. Scattering parameters for EXAFS fitting were generated using the FEFF8 software package.[44] The k^3-weighted data were fit in r space. The first coordination sphere was determined by setting the number of scattering atoms in each shell to integer values and systematically varying the combination of N/O and S donors (Tables S1 and S2 of the Supporting Information).

Multiple-scattering parameters for imidazole ligands bound to various metals were generated from crystallographic coordinates using the FEFF8 software package with previously published crystal structures as input.[46] The best fits resulted in four prominent multiple-scattering features, and paths of similar overall lengths were combined to make four imidazole scattering paths, matching these four prominent features as outlined by Costello et al.[47,48] The four combined paths were used to fit the data by setting the number of imidazole ligands per metal ion to integral values while allowing R and σ^2 to vary.[47,48] To compare different models of the same data set, the nonlinear least-squares fitting algorithm "ifeffit" (FEFF8) utilizes three goodness-of-fit parameters: χ^2, reduced χ^2, and the R factor. These parameters are not to be confused with nomenclature where R is used for interatomic distance and χ for k space EXAFS. The statistical parameter χ^2, which is minimized in a fit, is given by eq 1

$$\chi^2 = \frac{N_{idp}}{N_{\varepsilon^2}} \sum_{i=1}^{N} (\{\mathrm{Re}[\tilde{\chi}_{data}(R_i) - \tilde{\chi}_{model}(R_i)]\}^2 + \{\mathrm{Im}[\tilde{\chi}_{data}(R_i) - \tilde{\chi}_{model}(R_i)]\}^2) \quad (1)$$

where N_{idp} is the number of independent data points, N_{ε^2} is the number of uncertainties to minimize, Re() and Im() denote the real and imaginary parts of the EXAFS fitting function, respectively, and $\tilde{\chi}(R_i)$ is the Fourier-transformed data or model function: reduced $\chi^2 = \chi^2/(N_{idp} - N_{varys})$, where N_{varys} is the number of refining parameters and represents the degrees of freedom in the fit. Additionally, ifeffit calculates the R factor for each fit, which is directly proportional to χ^2 and a measure of the absolute misfit between the data and theory. The R factor is given by eq 2 and is scaled to the magnitude of the data making it proportional to χ^2.

$$R = \left[\sum_{i=1}^{N} (\{\mathrm{Re}[\tilde{\chi}_{data}(R_i) - \tilde{\chi}_{model}(R_i)]\}^2 + \{\mathrm{Im}[\tilde{\chi}_{data}(R_i) - \tilde{\chi}_{model}(R_i)]\}^2) \right] \Big/ \left[\sum_{i=1}^{N} \left(\left\{ \mathrm{Re}\left[\tilde{\chi}_{data_i}(R_i)\right] \right\}^2 + \{\mathrm{Im}[\tilde{\chi}_{data}(R_i)]\}^2 \right) \right] \quad (2)$$

Via comparison of different models, the R factor and reduced χ^2 parameter were used to determine which model was the best fit for the data. The R factor will generally improve with an increasing number of adjustable parameters, while reduced χ^2 will go through a minimum and then increase, indicating that the model is overfitting the data.[49]

dx.doi.org/10.1021/bi401132w | Biochemistry 2013, 52, 7689−7701

RESULTS

***Spn* PsaR Is a Homodimer in Solution Independent of Metallation State.** Wild-type $PsaR^{apo,apo}$, $PsaR^{Zn,apo}$, $PsaR^{Zn,Zn}$, and $PsaR^{Zn,Mn}$ were subjected to size exclusion chromatography with the elution profile analyzed by multiangle light scattering (MALS) to assess the homogeneity and quaternary structure of distinct metallation states of *Spn* PsaR (Figure 1). Representative experiments are shown for $PsaR^{apo,apo}$ (Figure 1A) and $PsaR^{Zn,apo}$ (Figure 1B) (≈160 μM protomer loaded onto the column, pH 7.0, 0.2 M NaCl), with the results shown for all wild-type PsaRs compiled in Table 1. Comparison of the elution profiles of $PsaR^{apo,apo}$ and $PsaR^{Zn,apo}$ reveals a trailing tail on a major peak for $PsaR^{apo,apo}$ that is not observed in $PsaR^{Zn,apo}$. The apparent molecular mass of $PsaR^{Zn,apo}$ is 48 kDa from this experiment (Table 1). The addition of a second molar protomer equivalent of metal, as Zn(II) or Mn(II), reveals no change in the elution pattern or measured assembly state (Table 1). These data support the conclusion that all forms of PsaR are homodimeric under these conditions and that the metal-free apo state may well be hydrodynamically somewhat larger and/or more structurally heterogeneous than metalated PsaRs, with Zn(II) binding to the high-affinity site (see below) quenching this heterogeneity. No evidence of monomeric PsaR was obtained in these profiles.

Table 1. Average Experimentally Determined Molecular Masses for Wild-Type *Spn* PsaR Loaded with Various Metals by MALS

PsaR metallation state[a]	molecular mass (Da)
monomer (reduced), expected	24852.6
dimer (reduced), expected	49705.2
$PsaR^{apo,apo}$	50000 ± 4000
$PsaR^{Zn,apo}$	48000 ± 1000
$PsaR^{Zn,Zn}$	47000 ± 3000
$PsaR^{Zn,Mn}$	47000 ± 2000

[a]Metallation state superscripts refer to the metal loaded in the site 1 (high affinity) followed by site 2 (low affinity). Solution conditions: 20 mM HEPES (pH 7.0), 200 mM NaCl, and 1 mM TCEP at ambient temperature; 150−160 μM protomer (100 μL) was used for each column run.

Mn(II) and Zn(II) Bind to the PsaR Dimer in Each of Two Distinguishable Steps. Following the determination of the dominant assembly state of wild-type PsaR, we next measured metal binding affinities and stoichiometries for both cognate Mn(II) and noncognate Zn(II). Chelator competition experiments were conducted with two different divalent metal ion competitors with vastly different affinities, mf2 (K_{Zn} = 5.0 × 10^7 M^{-1}) and quin-2 (K_{Zn} = 2.7 × 10^{11} M^{-1}), and the data were fit to the appropriate one-site or two-site binding model. Representative experiments are shown for the titration of a solution of wild-type PsaR and mf2 with Zn(II) (Figure 2A) or Mn(II) (Figure 2B). Both titrations can be satisfactorily fit to a 2:1 metal:protomer binding model (or four metal ions per dimer), with no need to invoke cooperativity of metal binding within the homodimer (Table 2). Thus, binding to site 1 and site 2 on each protomer is therefore considered an independent event. For Zn(II) binding, the first molar protomer equivalent of Zn(II) binds to PsaR because there is no change in the spectrum of the chelator; after that site is filled, Zn(II) binds to the second site in competition with mf2. Thus, only a lower limit for K_{Zn1} of ≥10^9 M^{-1} for site 1 can be obtained from this experiment; nonlinear least-squares fitting reveals a K_{Zn2} of (2.2 ± 0.5) × 10^8 M^{-1} (Table 2). To further estimate K_{Zn1}, a quin-2 competition experiment was performed (Figure 2C). Here, as with mf2 (Figure 2A), quin-2 provides little competition to PsaR for binding of Zn(II) to site 1; again, simulated curves (Figure 2C) reveal that only a lower limit for K_{Zn1} of ≥10^{13} M^{-1} can be obtained from this experiment (Table 2).

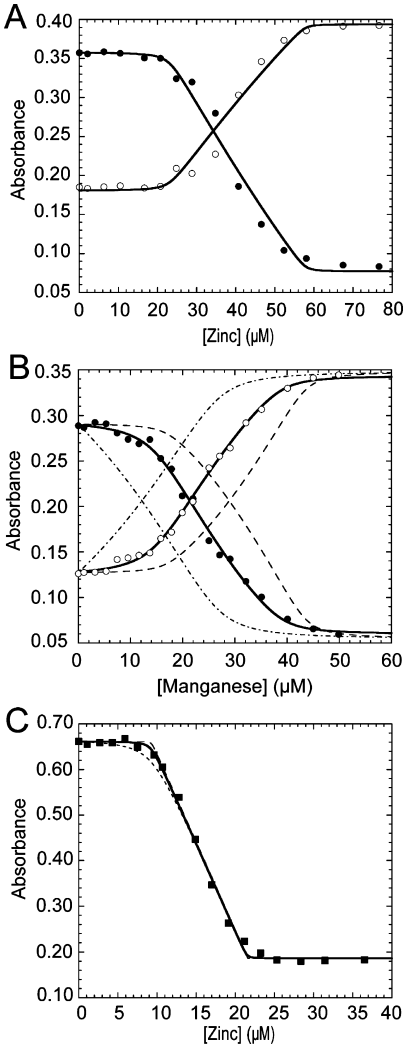

Figure 2. Representative isotherms obtained when a mixture of wild-type apo-PsaR and mag-fura-2 (mf2) (A and B; empty symbols for A_{325} and filled symbols for A_{360}) or quin-2 (C, filled symbols for A_{265}) is titrated with the indicated metal salt. (A) Titration of Zn(II) into mf2 (12 μM) and $PsaR^{apo,apo}$ (23 μM monomer). (B) Titration of Mn(II) into a solution of mf2 (10 μM) and PsaR (17 μM monomer). (C) Titration of zinc into a solution of quin-2 (12 μM) and PsaR (10 μM monomer). The solid lines represent a nonlinear global least-squares fit employing either a two-site (mf2) or a one-site (quin-2) competition model with the optimized binding parameters from multiple experiments listed in Table 2. The dashed lines in panels B and C represent simulated curves with each K_{Mn} (B) or K_{Zn} (C) 10-fold higher or 10-fold lower than the optimized value, for visual comparison with the fitted curves (Table 2).

The Mn(II) binding titrations of PsaR/mf2 (K_{Mn} = 2.4 × 10^6 M^{-1}) mixtures (Figure 2B), like those of Zn(II), can also be fit to two sites per protomer (or four per dimer) that bind Mn(II) with distinct affinities. In contrast to Zn(II), fitting of replicate binding isotherms reveals that both sites effectively compete with mf2, with a K_{Mn1} of (5.0 ± 0.2) × 10^7 M^{-1} and a K_{Mn2} of

dx.doi.org/10.1021/bi401132w | *Biochemistry* 2013, 52, 7689−7701

Table 2. Zn(II) and Mn(II) Binding Affinities for Sites 1 and 2 for Wild-Type and Mutant *Spn* PsaRs (pH 8.0, 0.2 M NaCl, 25 °C)[a]

Spn PsaR	log K_{Zn1} (M^{-1})	log K_{Zn2} (M^{-1})	log K_{Mn1} (M^{-1})	log K_{Mn2} (M^{-1})
wild-type	≥13[b]	8.35 ± 0.08	7.70 ± 0.07	6.09 ± 0.03
D7A (site 2)	≥9[c]	8.20 ± 0.06	5.15 ± 0.06	≤4[d]
E99A (site 2)	≥9[c]	7.97 ± 0.04	6.31 ± 0.04	≤4
H125A (site 1)	nd[e]	nd[e]	7.4 ± 0.1	6.61 ± 0.04
D160A (site 1)	≥9	7.88 ± 0.06	7.7 ± 0.1	6.62 ± 0.04
H76A	nd[e]	nd[e]	7.67 ± 0.08	5.73 ± 0.05
H76F	nd[e]	nd[e]	8.0 ± 0.2	6.39 ± 0.05

[a]Determined from mf2 competition experiments like those shown in Figure 2 unless otherwise noted. The standard errors in log *K* from three or more independent experiments are given. [b]Determined from a quin-2 competition experiment and represents a lower limit. [c]A lower limit can be determined only from these mf2 competition experiments.[40] [d]Could not be detected in mf2 competition experiment, and the number shown represents an upper limit. [e]Not determined because of protein precipitation under these conditions.

$(1.2 \pm 0.2) \times 10^6\ M^{-1}$ (Table 2). These results reveal that PsaR binds 2 molar protomer equivalents of Mn(II) or Zn(II), with Zn(II) binding preferentially to both sites 1 and 2, a general finding consistent with predictions from the Irving−William series of metal complex stabilities ($K_{Zn} \gg K_{Mn}$), with this preference far greater at site 1. In fact, the disparity between K_{Zn1} and K_{Mn1} (Table 2) and the absolute magnitude of K_{Zn1} suggest strongly that *in vivo*, site 1 is filled with zinc, which makes *Spn* PsaR a zinc metalloprotein. Interestingly, putative regulatory site 2 also favors zinc over manganese by ≈40-fold; thus, for PsaR to function as a Mn(II)-specific repressor in the cell, one would have to postulate that intracellular zinc concentrations do not increase under normal conditions to the point where Zn(II) would effectively compete with Mn(II) for occupancy of this site (see Discussion).

Structural Identification of Site 1 by X-ray Absorption Spectroscopy. We next exploited the finding that site 1 could be preferentially loaded with Zn(II) to prepare wild-type $PsaR^{Zn,apo}$ and $PsaR^{Zn,Mn}$ samples for analysis by X-ray absorption spectroscopy. This experiment provides structural information about the first coordination sphere of the site 1 Zn(II) and allows a determination of the degree to which filling site 2 with the cognate Mn(II) influences the structure of this site. Note that Mn(II) is transparent in this experiment. The zinc X-ray absorption near-edge spectra (XANES) are shown for $PsaR^{Zn,apo}$ (red trace) and $PsaR^{Zn,Mn}$ (blue trace) in Figure 3A, with the corresponding Fourier-transformed extended X-ray absorption fine structure (EXAFS) data and unfiltered k^3-weighted EXAFS spectra shown for $PsaR^{Zn,apo}$ (Figure 3B) and $PsaR^{Zn,Mn}$ (Figure 3C) samples. The threshold energy chosen for Zn was 9670 eV.[41] Edge normalization and background subtraction were performed using a Gaussian pre-edge function (between −200 and −50 eV with respect to E_o) and a second-order polynomial for the postedge region (between 150 and 861 eV with respect to ε_o) followed by normalization of the edge jump to 1.0. The normalized fluorescence intensity of the near edge increases with an increasing coordination number and assumes a value of ≈1.3 for four-coordinate structures and between 1.3 and 2.0 for five- and six-coordinate complexes, with six-coordinate complexes the most intense.[56] For

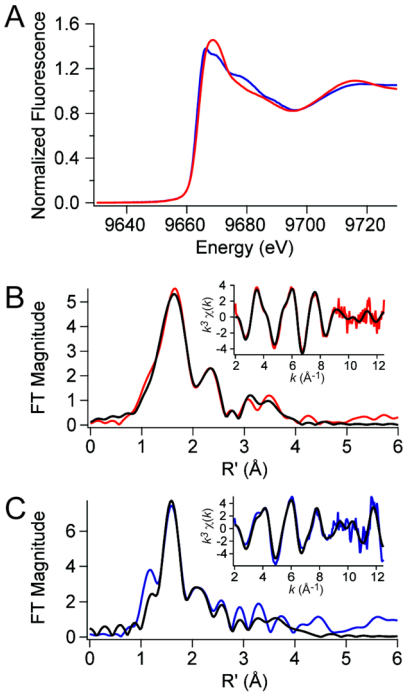

Figure 3. Zn K-edge X-ray absorption spectroscopy of wild-type $PsaR^{Zn,apo}$ (red traces) and $PsaR^{Zn,Mn}$ (blue traces). (A) Zinc XANES spectra for each species. (B) Fourier-transformed EXAFS data (main panel) obtained for $PsaR^{Zn,apo}$ (red trace) superimposed on best-fit coordination complex fits (black lines) as described by the parameters listed in Table 3. The inset shows the unfiltered k^3-weighted EXAFS spectrum and fits for $PsaR^{Zn,apo}$. (C) Fourier-transformed EXAFS data (main panel) obtained for $PsaR^{Zn,Mn}$ (blue trace) superimposed on best-fit coordination complex fits (black lines) (see Table 3). The inset shows the unfiltered k^3-weighted EXAFS spectrum and fits for $PsaR^{Zn,Mn}$.

$PsaR^{Zn,apo}$, the normalized intensity of ≈1.45 and an edge energy of ∼9663.9 eV are more consistent with a five-coordinate complex. However, for $PsaR^{Zn,Mn}$, the normalized intensity of ≈1.38 and an edge energy of ∼9663.3 eV are more consistent with a four-coordinate complex.

These conclusions are consistent with the EXAFS analysis (Figure 3B,C and Table 3) and a nonlinear least-squares analysis of the EXAFS data (black solid curves in Figure 3B,C). Fitted parameters from the best fit, as judged by minimizing % *R* and χ^2 and optimizing meaningful σ^2 values, are compiled in Table 3 (the results of other fits are shown in Tables S1 and S2 of the Supporting Information). The best fit for $PsaR^{Zn,apo}$ is a five-coordinate complex composed of four N/O donor ligands at 2.05 Å, with one from an imidazole (histidine) ligand (as evidenced by the spectral features at r = 3−4 Å), and a single sulfur (S) scatterer 2.31 Å from the Zn(II). The presence of a single S donor suggests that high-affinity site 1 in PsaR is analogous to the Cd(II) site previously observed in *Sgo* ScaR formed by conserved residues Glu80, Cys123, His125, and Asp160, with one of the carboxylate ligands adopting bidentate coordination. In contrast, addition of Mn(II) to site 2 in $PsaR^{Zn,apo}$ to form $PsaR^{Zn,Mn}$ is best fit by a four-coordinate complex featuring one fewer N/O donor, but otherwise likely involving the same donor residues. A five-coordinate fit, while also acceptable, returns a fit statistically poorer than that of the four-coordinate fit (Table S2 of the Supporting Information). These data taken collectively reveal Mn(II) binding to site 2

dx.doi.org/10.1021/bi401132w | *Biochemistry* 2013, 52, 7689−7701

Table 3. Zinc XANES and EXAFS Analysis for Wild-Type PsaR^{Zn,apo} and Wild-Type PsaR^{Zn,Mn}

		XANES analysis		EXAFS analysis			
metal ion	K-edge energy (eV)	CN[a]	shell[b]	r (Å)	σ^2 ($\times 10^{-3}$ Å^2)	ΔE_o (eV)	% R
			PsaR^{Zn,apo}				
Zn(II)	9663.9	5	4 N/O (1 Im)	2.05 (1)[c]	8 (1)	−5 (1)	1.14
			1 S	2.31 (1)	6 (1)		
			PsaR^{Zn,Mn}				
Zn(II)	9663.3	4	3 N/O (1 Im)	2.03 (1)	2 (1)	3 (3)	5.19
			1 S	2.37 (2)	3 (2)		

[a]Coordination number. [b]Im, number of imidazole (histidine) ligands among N/O donors. [c]The estimated uncertainties in the corresponding parameters in the last significant figure are given. These uncertainties were calculated by SixPack and reflect the change in the variable that will result in an increase in χ^2 of 1.0.

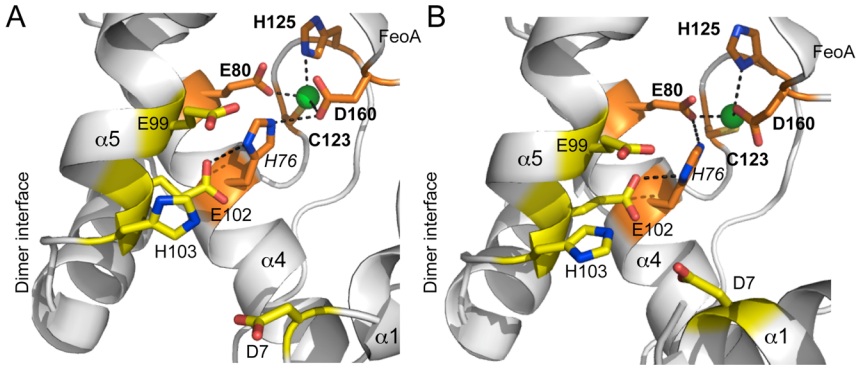

Figure 4. Close-up view of Cd(II) site 1 in each of the two subunits (A and B) in *Sgo* ScaR (Protein Data Bank entry 3HRT)[34] (ligating residues colored orange; E80, C123, H125, and D160), emphasizing the physical location of H76 and immediately adjacent candidate regulatory site 2 ligands D7, E99, E102, and H103 (yellow). Side chains are shown as sticks in elemental shading; the Cd(II) ion is shown as a green sphere. Note that the homodimer is strongly asymmetric, and this asymmetry extends to the metal site region that adopts distinct structures in each protomer. D7 approaches the other candidate site 2 ligands more closely in the α5 helix in the right (B) protomer relative to the left (A). Note also metal coordination bonds are unreasonably long in all cases, likely attributed to the modest resolution (2.7 Å) of the structure.

induces a detectable change in the first coordination sphere of the Zn(II) bound in site 1 (Table 3). The structural basis of this rearrangement is of course not known but could be accomplished by a change in bidentate to monodentate coordination by Glu80, which is bidentate in the *Sgo* ScaR Cd(II)-bound structure and is closest to the proposed regulatory site ligands (*vide infra*). In any case, these two metal sites in the PsaR dimer clearly communicate with one another and may be reporting on a more global conformational transition associated with binding of the cognate metal to site 2.

Metal Binding Properties of PsaR Mutants. Having established the order of metal ion binding and structural identification of site 1 as the metal site positioned between the dimerization and FeoA domains, we next determined the metal [Zn(II) and Mn(II)] binding affinities and stoichiometries for two putative site 1 nonliganding mutants (H125A and D160A), two candidate site 2 mutants from a multiple-sequence alignment of MntR, DtxR, and PsaR [D7A and E99A (Figure S1 of the Supporting Information)], and two His76 mutants (H76F and H76A). His76 is not a predicted ligand to either metal in PsaR but is a direct ligand to the ancillary metal ion in DtxR and to the A site Mn(II) in MntR and is absolutely conserved. In the ScaR structure, H76 appears to "bridge" site 1 (via Glu80 or D160) and candidate site 2 (Glu102) residues via hydrogen bonding, on the basis of the inspection of the two Cd(II) complexes in the *Sgo* ScaR dimer structure (Figure 4). The prediction is that mutation of His76 would disrupt the allosteric linkage between DNA and the cognate regulatory site, with no effect on the metal binding affinities. We used the same chelator competition assays with mf2 to assess binding parameters for Zn(II) and Mn(II) exactly as described above for wild-type PsaR, with all results summarized in Table 2. Site 1, site 2, and His76 mutants are discussed in turn.

Both H125A and D160A PsaR site 1 mutants bind 2 molar protomer equivalents of Mn(II) with the K_{Mn} for both site 1 and site 2 within a factor of 2−3 of that of wild-type PsaR (Table 2). Although Zn(II) binding measurements for H125A PsaR could not be taken because of extensive protein precipitation, the affinity of D160A PsaR for Zn(II) is within a factor of ≈2 of that of wild-type PsaR at low-affinity site 2 (K_{Zn2} = 7.6 × 10^7 M^{-1}), with only a lower limit obtained for high-affinity site 1 ($K_{Zn1} \geq 10^9$ M^{-1}). Thus, to a first approximation, single-amino acid substitutions in site 1 have only weak effects on metal binding to either site, with the possible exception of binding of Zn(II) to site 1 (Table 2).

In contrast, both D7A and E99A candidate site 2 mutants exhibit the shared characteristic of dramatically lowering the cognate Mn(II) affinity of both sites, with correspondingly little effect on noncognate Zn(II) binding affinity. K_{Zn1} remains too tight to measure in mf2 competition experiments, with a K_{Zn2} of ≈10^8 M^{-1}, essentially as described for wild-type PsaR (Table 2). For Mn(II), in contrast, only one binding site is competitive with mf2 (which we attribute to high-affinity site 1) but is characterized by K_{Mn1} values that are 200-fold (D7A PsaR) and 20-fold (E99A PsaR) weaker than that of wild-type PsaR. The second Mn(II) binding event cannot be observed in either D7A or E99A PsaRs; i.e., $K_{Mn2} \leq 10^4$ M^{-1} under these conditions (Table 2).

dx.doi.org/10.1021/bi401132w | *Biochemistry* 2013, 52, 7689−7701

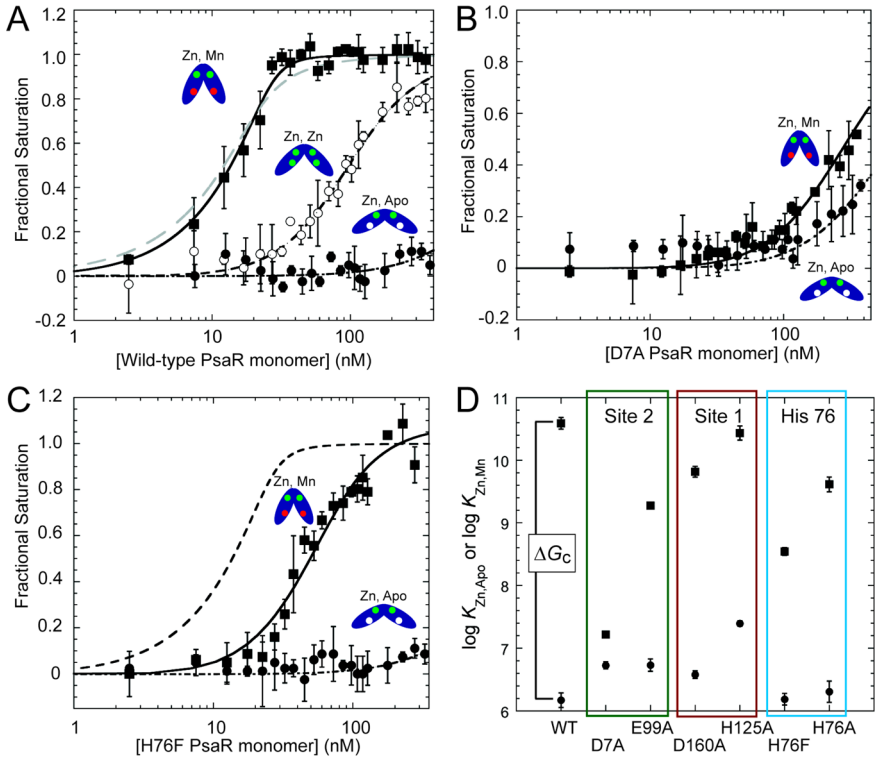

Figure 5. DNA binding isotherms for various metalated states of wild-type PsaR (A), D7A PsaR (B), and H76F PsaR (C). In each case, data for $PsaR^{Zn,apo}$, $PsaR^{Zn,Zn}$, and $PsaR^{Zn,Mn}$ species are shown as filled circles, empty circles, and filled squares, respectively. The smooth curves through each data set correspond to those derived from a dissociable dimer binding model (see Materials and Methods for details), with K_{DNA}^{i} values complied in Table 4. The gray dashed line in panel A shows the fit for a nondissociable dimer model for PsaR binding (see Table 4). The dashed line in panel C shows the fit for wild-type $PsaR^{Zn,Mn}$ for comparison only. (D) Summary of the DNA binding affinities of $PsaR^{Zn,apo}$ (●) and $PsaR^{Zn,Mn}$ (■) for wild-type PsaR and indicated mutants with the vertical separation between these K_i values proportional to ΔG_c from the relationship $\Delta G_c^{Mn} = -RT \ln(K_{DNA}^{Zn,Mn}/K_{DNA}^{Zn,apo})$ or for Zn(II) $\Delta G_c^{Zn} = -RT \ln(K_{DNA}^{Zn,Zn}/K_{DNA}^{Zn,apo})$. ΔG_c is equivalent to a $\Delta\Delta G$, or the difference in PsaO DNA binding free energy between the appropriate metalated form ($PsaR^{Zn,Mn}$ or $PsaR^{Mn,Mn}$) and $PsaR^{Zn,apo}$.

Characterization of the metal binding properties of candidate allosteric mutants H76F and H76A PsaRs reveals that each binds 2 molar protomer equivalents of Mn(II) (Table 2) with largely indistinguishable affinities, e.g., within a factor of 2−3 of that of wild-type PsaR. Zn(II) binding affinities could not be confidently measured under these conditions because of complications from precipitation of the high protein concentration required by this experiment. This did not preclude quantitative DNA binding experiments for extracting ΔG_c (Figure 5), which are described below. In any case, these data suggest to a first approximation that substitution of His76 has an only weak effect on metal binding affinities, much like the site 1 mutants (Table 2).

DNA Operator Binding by Various Metalated Wild-Type and Mutant PsaRs. Having determined the cognate Mn(II) and noncognate Zn(II) binding affinities and stoichiometries for wild-type PsaR and various site 1, site 2, and H76 mutants, we next quantified the degree to which each metalated species is capable of metal-dependent [Mn(II) vs Zn(II)] allosteric positive regulation of *psaBCA* operator (PsaO) binding. To do this, we conducted quantitative DNA binding assays by monitoring the anisotropy of the fluorescence of a 32 bp fluorescein-labeled PsaO-containing duplex (10 nM) in a 96-well microtiter plate format with each point in a binding curve measured in triplicate. The DNA binding affinities (K_{DNA}) were determined for all four metalated states of wild-type PsaR (Figure 5A and Table 4), i.e., $PsaR^{apo,apo}$, $PsaR^{Zn,apo}$, $PsaR^{Zn,Zn}$, and $PsaR^{Zn,Mn}$, while for all other mutant proteins, only $PsaR^{Zn,apo}$ and $PsaR^{Zn,Mn}$ were measured (Figure 5 and Table 4). The allosteric coupling free energy, ΔG_c, was then determined from these K_{DNA} values as a measure of the degree to which cognate Mn(II) or noncognate Zn(II) bound to site 2 allosterically activates DNA binding upon saturation of site 2 relative to an empty site 2 [with site 1 filled with Zn(II) in all cases, $PsaR^{Zn,apo}$] (Table 4).

Inspection of these binding isotherms for wild-type PsaR (Figure 5A) shows clearly that apo PsaR, $PsaR^{Zn,apo}$, binds weakly under these conditions (pH 8.0, 0.2 M NaCl) as expected and that noncognate Zn(II), while capable of activating PsaO binding when bound to site 2 ($PsaR^{Zn,Zn}$), is far less effective than cognate Mn(II). Analysis using a dimer linkage model and assuming the same K_{dimer} in each species reveals an ≈380-fold decrease in the PsaO affinity of the noncognate $PsaR^{Zn,Zn}$ complex versus that of the cognate $PsaR^{Zn,Mn}$ complex (Table 4) and does not give rise to significant activation until a protein concentration reaches a level at which the Mn(II)-bound form saturates the DNA. The Gibbs coupling free energy, ΔG_c, operationally defined as described in the legend of Table 4, is more than 2-fold greater for Mn(II) than for Zn(II) bound to site 2 (−6.0 vs −2.5 kcal mol^{-1} under these conditions). Interestingly, $PsaR^{Mn,Mn}$ is slightly less capable than $PsaR^{Zn,Mn}$ of driving allosteric activation of PsaO binding, although the difference is small (ΔG_c = −5.3 kcal mol^{-1}) (Table 4). Although this operationally defined value of ΔG_c is obviously dependent upon the value measured for K_{dimer},[40] there is clearly some detectable linkage to

dx.doi.org/10.1021/bi401132w | *Biochemistry* 2013, 52, 7689−7701

Table 4. DNA Binding Affinities of the Indicated Metalated Derivatives of Wild-Type and Mutant PsaRs As Analyzed by a Dimer Linkage Model[a]

Spn PsaR	log K_{DNA} (M^{-1})	fractional change in K_{DNA} from that of corresponding wild-type PsaR	ΔG_c (kcal mol^{-1})
wild-type $PsaR^{Zn,apo}$	6.2 ± 0.1	*1*	–
wild-type $PsaR^{Zn,Zn}$	8.02 ± 0.03	0.0027[b]	−2.5 ± 0.2[d]
wild-type $PsaR^{Zn,Mn}$	10.6 ± 0.1	1	−6.0 ± 0.3[d]
wild-type $PsaR^{Mn,Mn}$	10.1 ± 0.1	0.30	−5.4 ± 0.4[d]
D7A $PsaR^{Zn,apo}$	6.73 ± 0.05	*3.6*[c]	–
D7A $PsaR^{Zn,Mn}$	7.22 ± 0.03	0.00042	−0.7 ± 0.1[e]
E99A $PsaR^{Zn,apo}$	6.7 ± 0.1	*3.6*	–
E99A $PsaR^{Zn,Mn}$	9.27 ± 0.05	0.048	−3.5 ± 0.2[e]
H125A $PsaR^{Zn,apo}$	7.39 ± 0.04	*16*	–
H125A $PsaR^{Zn,Mn}$	10.4 ± 0.1	0.71	−4.1 ± 0.2[e]
D160A $PsaR^{Zn,apo}$	6.58 ± 0.06	*2.5*	–
D160A $PsaR^{Zn,Mn}$	9.8 ± 0.1	0.17	−4.4 ± 0.2[e]
H76A $PsaR^{Zn,apo}$	6.3 ± 0.2	*1.4*	–
H76A $PsaR^{Zn,Mn}$	9.6 ± 0.1	0.11	−4.5 ± 0.4[e]
H76F $PsaR^{Zn,apo}$	6.2 ± 0.1	*1.0*	–
H76F $PsaR^{Zn,Mn}$	8.54 ± 0.06	0.0089	−3.2 ± 0.2[e]

[a]Determined from experiments like those shown in Figure 5 with the errors defined as the unweighted standard errors of the fits from triplicate titrations. [b]The numbers in standard text are calculated from K_{DNA}(mutant $PsaR^{i,j}$)/K_{DNA}(wild-type $PsaR^{Zn,apo}$), where i = j = Zn or Mn. [c]The numbers in italics are given by the ratio K_{DNA}(mutant $PsaR^{Zn,apo}$)/K_{DNA}(wild-type $PsaR^{Zn,apo}$). [d]$\Delta G_c = -RT \ln[K_{DNA}(\text{wild-type } PsaR^{i,j})/K_{DNA}(\text{wild-type } PsaR^{Zn,apo})]$, where i = j = Zn or Mn. [e]$\Delta G_c = -RT \ln[K_{DNA}(\text{mutant } PsaR^{Zn,Mn})/K_{DNA}(\text{mutant } PsaR^{Zn,apo})]$.

the monomer−dimer equilibrium as a fit to a nondissociable dimer binding model for $PsaR^{Zn,Mn}$ does not fit nearly as well (Figure 5A, gray dashed line). This justifies use of this simple linkage model in analyzing all subsequent binding isotherms.

Both site 1 mutations, H125A and D160A, significantly lower ΔG_c to ≈4 kcal mol^{-1} or by ∼35% relative to that of wild-type PsaR and thus have a detectable influence on allosteric linkage (Table 4) in the absence of large changes in Mn(II) binding affinity (Table 2). The underlying origins are different, however, in the two mutants. For H125A PsaR, the apo form ($PsaR^{Zn,apo}$) binds the operator DNA ≈10-fold more tightly than wild-type PsaR, while the fully activated affinity of $PsaR^{Zn,Mn}$ is indistinguishable from that of wild-type PsaR (Figure 5D and Table 4). In contrast, in D160A PsaR, the apoprotein affinity is only 2-fold higher, with a fully activating affinity of $PsaR^{Zn,Mn}$ ≈8-fold lower than that of wild-type PsaR. The characteristics of these mutants reveal that mutations in metal site 1 disrupt allosteric switching, which itself is strongly dependent on the occupancy of site 2 with cognate Mn(II); i.e., the structural integrity of both sites is required for full allosteric activation of PsaO binding by PsaR (Figure 5D).

Like the two site 1 mutants, both site 2 mutants, D7A and E99A PsaRs, have similar DNA binding characteristics; however, the D7A mutant is far more functionally compromised than E99A PsaR. In fact, these findings generally track with the relative perturbations in metal site affinities for each mutant (*vide supra*, Table 2). Both mutants bind the PsaO with a slightly elevated affinity in the absence of activating metal ($PsaR^{Zn,apo}$) (Figure 5D and Table 4); however, the D7A mutation essentially abrogates Mn(II)-dependent activation of PsaO binding with a ΔG_c for $PsaR^{Zn,Mn}$ of −0.7 kcal mol^{-1} under these conditions (see also Figure 5C). E99A PsaR is also severely functionally compromised, although the $PsaR^{Zn,Mn}$ form binds ≈100-fold more strongly to the PsaO than D7A PsaR, giving a ΔG_c for E99A $PsaR^{Zn,Mn}$ of −3.2 kcal mol^{-1} or ≈50% of that of wild-type PsaR. We conclude that the structural integrity of site 2 is critically tied to allosteric switching, with the candidate ligand derived from near the N-terminus, D7, playing a major role in this process.

Finally, characterization of the predicted allosteric switching mutants H76A and H76F PsaRs reveals that H76 functions in some way in this process. Both $PsaR^{Zn,apo}$ mutants bind the PsaO with wild-type-like low affinities (Table 4 and Figure 5C), but each is distinct in allosteric activation of the $PsaR^{Zn,Mn}$ forms. Interesting, the H76F PsaR mutant (Figure, 5C) is far more functionally compromised than H76A PsaR, with an activation potential comparable to that of E99A PsaR (ΔG_c = −3.2 kcal mol^{-1}), with the H76A mutant most quantitatively similar to site 1 mutant D160A PsaR (ΔG_c = −4.5 kcal mol^{-1}). The characterization of these two H76 mutants highlights the potential impact of the second coordination shell on metal complexation of site 1 (see Figure 4), site 2, or both in moving from $PsaR^{Zn,apo}$ to the activated $PsaR^{Zn,Mn}$ state.

DISCUSSION

In this work, we elucidate the quaternary structure, metal binding and DNA binding properties of *Spn* PsaR, a member of an emerging subclass of Mn(II)-sensing repressors in the DtxR/MntR metalloregulator family.[4] PsaR is a stable homodimer at a high concentration (≈160 μM) irrespective of the metallation state, consistent with previous studies of both *Bsu* MntR and *Sgo* ScaR.[29,34] We establish that the PsaR homodimer harbors two pairs of divalent metal binding sites (four per dimer) that are functionally nonequivalent and structurally distinct. High-affinity site 1 that straddles the dimerization and FeoA domains is likely filled by Zn(II) in the cell given $K_{Zn1} \geq 10^{13}$ $M^{-1} \gg K_{Mn1}$, thus establishing that PsaR is a zinc metalloprotein. The occupancy of this site by Zn(II) or Mn(II) is necessary for full activation by Mn(II) but keeps PsaR in an inactive DNA binding state. It is only when lower-affinity site 2 is bound by cognate Mn(II) that $PsaR^{Zn,Mn}$ is maximally activated to bind to PsaO (Figure 5). Binding of Zn(II) to site 2 is weakly effective in allosteric activation, despite a higher binding affinity, and $PsaR^{Zn,Zn}$ is characterized by an allosteric coupling free energy that is only 40% of that of $PsaR^{Zn,Mn}$. High-affinity metal site 1 is unique to the streptococcal clade of DtxR/MntR repressors. The two metal binding sites in PsaR clearly communicate with one another because mutations of ligating residues in site 1 significantly diminish ΔG_c while mutations in activating metal site 2 significantly alter the affinity of Mn(II), and perhaps Zn(II), for site 1. Furthermore, the occupancy of cognate Mn(II) in site 2 detectably alters the first coordination sphere around the Zn(II) ion bound to site 1 (Figure 3 and Table 3), which may

dx.doi.org/10.1021/bi401132w | *Biochemistry* 2013, 52, 7689−7701

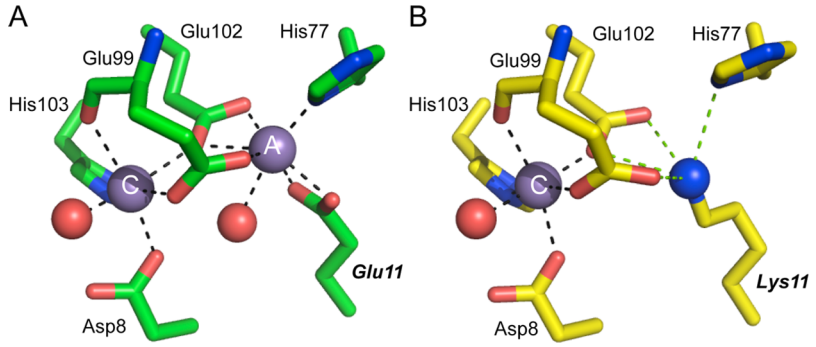

Figure 6. Comparison of the Mn(II)-bound chelate regions of wild-type MntR [Protein Data Bank (PDB) entry 2F5D][32] (A) and E11K MntR (PDB entry 4HX4)[33] (B). The A and C Mn(II) ions are indicated in each panel, and all residues are shown as sticks. Coordination bonds are represented by black dashed lines, with potential electrostatic interactions deriving the ϵNH_2 group of Lys11 in E11K PsaR shown as green dashed lines in panel B. All residues are conserved in PsaR with identical residue numbers except that His77 is His76 in PsaR (see the text for details). E11K MntR[33] (B) is an excellent model for the Mn(II) bound in site 2 in PsaR (this work).

or may not be mediated by the "bridging" H76 and E80 in site 1 (Figure 4).

One striking finding is that the Mn(II) binding affinity of regulatory site 2 in PsaR measured here at pH 8.0 and 0.2 M NaCl [K_{Mn2} = (1.2 ± 0.2) × 10^6 M^{-1} ($K_{d,Mn2}$ = 0.83 μM)] is ≈10-fold larger that that directly measured for the two sites in MntR[32,51] and for *Sgo* ScaR[34] under similar conditions and at the same pH. In contrast, the Zn(II) affinities of all three proteins are more similar than different and in the range of 10^7−10^8 M^{-1}. The set-point model for metal sensing in the cell posits that the dissociation constant (K_d) of the regulator for its cognate metal establishes the intracellular bioavailability or "free" concentration, e.g., $[Mn]_{free}$, in the cell.[52] As a result, one could hypothesize that *S. pneumoniae* maintains a smaller bioavailable pool of Mn(II) than does *B. subtilis*. Total cell-associated Mn(II) is on par with total cell-associated Zn(II) in *S. pneumoniae* and significantly greater than total cell-associated Fe(II),[18] but to the best of our knowledge, similar measurements have not yet been reported for *B. subtilis*. In any case, with relatively few annotated Mn(II)-specific metalloenzymes in *S. pneumoniae*, including a Mn(II) SodA,[53] SapH,[54] PhpP, PpaC, and CpsB,[55] we hypothesize that much of the cell-associated Mn(II) may be bioavailable in low-molecular mass complexes as found in other bacteria.[14] This may well protect the pneumococcus from endogenous and exogenous oxidative damage and from immune system killing.[19] Modest Zn(II) toxicity is known to reduce cell-associated Mn(II) levels by ≈40%, which gives rise to strong upregulation of the PsaR regulon;[18,19,56] this suggests the formal possibility that under these conditions, Zn(II) effectively competes with Mn(II) and drives PsaR off the DNA as a result of its lower ΔG_c (Figure 5 and Table 4). For this to happen inside the cell, $[Zn]_{free}$ would have to rise only into the ≈0.01 μM range under these conditions; this seems possible given the modest (≈10^7−10^8 M^{-1}) affinity of the zinc efflux regulator SczA for Zn(II) (G. Campanello and D. Giedroc, unpublished results).[52] Direct measurement of $[Zn]_{free}$ is required to substantiate the proposal that excess intracellular Zn(II) causes misregulation of PsaR function in the cell.

The general finding of two pairs of functionally non-equivalent metal sites is also found in the Fe(II) sensor DtxR. Here, an ordered or stepwise binding to a higher-affinity ancillary site 1 is required for complete activation of DNA binding, but metal specificity is achieved by binding of a cognate metal to a lower-affinity site 2, which incorporates a ligand analogous to D7 (M8 in DtxR) from the DNA binding domain.[22] DtxR contains a Met (M8) and Cys (C102; often substituted with D in crystallographic studies) at positions corresponding to D7 and E99, respectively, in PsaR studied here; M8 is a clear metal specificity determinant when one compares DtxR and MntR using both structural and biological approaches.[25,57] The molecular details of allosteric activation by Fe(II) or other divalent metal ions bound to site 2 have been the subject of much discussion since the original structure of the Ni(II)-activated C102D DtxR bound to the *tox* operator-promoter was reported[58] and may well involve a coil-to-helix transition in helix α1 harboring M8 [D7 in PsaR (see Figure 4)].[58] In MntR, Mn(II) binding strongly stabilizes helix α1 [which harbors two metal ligands to each of the A and C sites of the binuclear Mn(II) cluster (see Figure 6A)] against H−D exchange relative to the apo state[59] and limits the conformational disorder of the DNA-binding domain relative to the dimerization domain.[24] In any case, what seems clear is that direct coordination by M8 in DtxR/IdeR and D7 in MntR by the activating metal drives a global "caliper-like" closure of the DNA-binding domains in each subunit relative to one another (Figure S1 of the Supporting Information), which brings them into alignment to bind to successive major grooves in the DNA operator.[24,33,58,60,61] A globally similar mechanism almost certainly characterizes PsaR given the essentiality of D7 to allosteric activation of PsaO binding (Table 4 and Figure 5) and the finding that each empty site 2 of the "apo" structure of *Sgo* ScaR adopts a distinct structure with D7 more closely approaching the bound metal site 1 (Figure 4). Also of interest is the early finding that the C-terminal SH3 domain of DtxR (not found in MntR) makes direct contact with site 1 metal ligands and the winged helical domain in the metal-activated DNA-bound form of DtxR,[60] thus potentially quantitatively influencing allosteric activation in that system. It is unclear what role the FeoA domain in PsaR might play in this process except to say that mutagenesis of metal site 1 ligand D160, found in the loop between the dimerization and FeoA domains, reduces the allosteric coupling free energy by ≈35% (Table 4).

The C site Mn(II) complex in MntR is likely an excellent model for activating site 2 in PsaR, because D8, E99, E102, and H103 in MntR precisely correspond to D7, E99, E102, and H103, respectively, in PsaR (Figure 6). The coordination geometry of the C site can be described as distorted octahedral, which involved monodentate coordination by each of these four side chains, in addition to the backbone carbonyl oxygen

atom of E99 and a water molecule (Figure 6A). Recent experiments reveal that the A site metal cation can be functionally replaced by the ε-NH_3^+ group of Lys11 in an E11K mutant; further, substitution of the only nonbridging ligand to the A site, H77, with Ala, still results in specific Mn(II)-dependent allosteric activation upon occupation of the C site (Figure 6B). Strikingly, *Sgo* ScaR and *Spn* PsaR and closely related streptococcal Mn(II) sensors harbor a Lys residue in this position, while Fe(II) sensors DtxR and IdeR harbor an Arg here (Figure S1C of the Supporting Information); this would be predicted to destroy the A site-like metal binding in PsaR, which is dependent on E99 and E102 bridging the A and C sites, with His76 completing the A site coordination complex (Figure 6A).[33] These studies provide strong support for the conclusion that *Spn* PsaR is simply a C site single-Mn(II) variant of *Bsu* MntR (Figure 6B).[33] The strongly functionally compromised D7A and E99A PsaRs are fully consistent with this conclusion, with D7 Mn(II) coordination being absolutely required for the Mn(II)-dependent activation. Finally, it is interesting to note that H77 in MntR corresponds precisely to His76 in PsaR, and the analogous H76A and H76F PsaRs are functionally compromised, without donation of the metal−ligand bond to either metal, although to differing degrees (Figure 5 and Table 4). The location of the H76 side chain between site 1 and site 2 in PsaR suggests that it may function as an important part of a network that effectively forces the PsaR homodimer to undergo a transition to a high-affinity DNA binding state when Mn(II) is loaded into site 2 (Figure 4).

Why is Zn(II) not a potent allosteric activator in PsaR? There is significant support for the hypothesis that distinct coordination environments of cognate versus noncognate metal complexes in metal sensor proteins of widely disparate structures are key determinants of the functional selectivity in the cell.[25,35,40,41,62−67] This may not, however, be the case for all metallosensors,[36,51,68] and in these cases, the influence of cellular metal bioavailability is likely a major factor that controls metal sensing so that illegitimate cross-talk between metal homeostasis systems can be avoided.[2,51,57,69,70] This hypothesis predicts that Mn(II) would adopt a coordination geometry that is distinct from that of Zn(II). We do not yet know the coordination chemistries around either Mn(II)- or Zn(II)-bound regulatory site 2; however, it is the case that substitution of D7 (and E99) with Ala produces a substantial ≥100-fold decrease in the Mn(II) binding affinity, while the Zn(II) binding affinity of site 2 is only minimally, if at all, affected (Table 2). This suggests the possibility that Zn(II) does not stably recruit D7 into a lower-coordination number complex, making a caliper-like closure of the DNA-binding domains far less energetically favorable and thus reducing ΔG_c for Zn(II) over cognate Mn(II). It is the case that the Zn(II) affinity of site 2 in PsaR is quite modest ($\approx 10^8$ M^{-1}), which might imply a smaller set of protein-derived ligands to this noncognate metal. In *Bsu* MntR, the structure of Zn(II)-bound MntR reveals that helix α1 is unwound and Asp7 is not coordinated to what would be the C site Zn(II), because Zn(II) is bound only to the A site in wild-type MntR (see Figure 6A).[32] The coordination structure of the Mn(II)-sensing complex of PsaR is not yet known but likely adopts a six-coordinate C site-like complex exactly like found in the binuclear wild-type and mononuclear E11K MntRs (Figure 6A).[32,33] EPR studies should allow us to determine this structure, with the mixed metal $PsaR^{Zn,Mn}$ species being an ideal target for these studies.[71] High-resolution crystallographic studies will be required to elucidate further the structural basis of allosteric regulation of PsaR and, in particular, the key roles played by Asp7 and the "bridging" residue His76 in driving this allosteric switch, as well as its ability to distinguish Mn(II) from Fe(II) and thereby regulate cross talk between these two metals in the cell.[51,72] These future studies will have implications for understanding how Mn(II) homeostasis impacts microbial physiology and virulence of this important human pathogen.

■ ASSOCIATED CONTENT

Supporting Information

Figures S1−S4 and Tables S1 and S2. This material is available free of charge via the Internet at http://pubs.acs.org.

■ AUTHOR INFORMATION

Corresponding Author

*E-mail: giedroc@indiana.edu. Phone: (812) 856-3178.

Funding

Funding was provided by National Institutes of Health (NIH) Grants GM042569 (D.P.G.), GM097225 (D.P.G.), and GM069696 (M.J.M.) and a fellowship awarded by the Graduate Training Program in Quantitative and Chemical Biology at Indiana University (J.P.L.). The National Synchrotron Light Source (NSLS) at Brookhaven National Laboratory is supported by the U.S. Department of Energy, Division of Materials Sciences and Division of Chemical Sciences. Beamline X3B at NSLS is supported by the NIH. This publication was made possible by Center for Synchrotron Biosciences Grant P30-EB-009998 from the National Institute of Biomedical Imaging and Bioengineering.

Notes

The authors declare no competing financial interest.

■ ACKNOWLEDGMENTS

We thank Dr. Crisjoe Joseph, Heidi Hu,and Carolyn Carr from the Maroney laboratory for XAS data collection, Dr. Todd Stone for the training on and use of the DAWN HELEOS II and OptiLab rEX instruments at the Indiana University Physical Biochemistry Instrumentation Facility, and Dr. Lichun Li (Indiana University) for training and use of the Biotek Synergy H1 Hybrid Multi-Mode Microplate reader.

■ REFERENCES

(1) Andreini, C., Bertini, I., Cavallaro, G., Holliday, G. L., and Thornton, J. M. (2008) Metal ions in biological catalysis: From enzyme databases to general principles. *J. Biol. Inorg. Chem. 13*, 1205−1218.

(2) Waldron, K. J., Rutherford, J. C., Ford, D., and Robinson, N. J. (2009) Metalloproteins and metal sensing. *Nature 460*, 823−830.

(3) Klein, J. S., and Lewinson, O. (2011) Bacterial ATP-driven transporters of transition metals: Physiological roles, mechanisms of action, and roles in bacterial virulence. *Metallomics 3*, 1098−1108.

(4) Ma, Z., Jacobsen, F. E., and Giedroc, D. P. (2009) Coordination Chemistry of Bacterial Metal Transport and Sensing. *Chem. Rev. 109*, 4644−4681.

(5) Imlay, J. A. (2013) The molecular mechanisms and physiological consequences of oxidative stress: Lessons from a model bacterium. *Nat. Rev. Microbiol. 11*, 443−454.

(6) Corbin, B. D., Seeley, E. H., Raab, A., Feldmann, J., Miller, M. R., Torres, V. J., Anderson, K. L., Dattilo, B. M., Dunman, P. M., Gerads, R., Caprioli, R. M., Nacken, W., Chazin, W. J., and Skaar, E. P. (2008) Metal chelation and inhibition of bacterial growth in tissue abscesses. *Science 319*, 962−965.

(7) Kehl-Fie, T. E., Chitayat, S., Hood, M. I., Damo, S., Restrepo, N., Garcia, C., Munro, K. A., Chazin, W. J., and Skaar, E. P. (2011) Nutrient metal sequestration by calprotectin inhibits bacterial superoxide defense, enhancing neutrophil killing of *Staphylococcus aureus*. *Cell Host Microbe 10*, 158−164.
(8) Kehl-Fie, T. E., Zhang, Y., Moore, J. L., Farrand, A. J., Hood, M. I., Rathi, S., Chazin, W. J., Caprioli, R. M., and Skaar, E. P. (2013) MntABC and MntH contribute to systemic *Staphylococcus aureus* infection by competing with calprotectin for nutrient manganese. *Infect. Immun. 81*, 3395−3405.
(9) Damo, S. M., Kehl-Fie, T. E., Sugitani, N., Holt, M. E., Rathi, S., Murphy, W. J., Zhang, Y., Betz, C., Hench, L., Fritz, G., Skaar, E. P., and Chazin, W. J. (2013) Molecular basis for manganese sequestration by calprotectin and roles in the innate immune response to invading bacterial pathogens. *Proc. Natl. Acad. Sci. U.S.A. 110*, 3841−3846.
(10) Anjem, A., Varghese, S., and Imlay, J. A. (2009) Manganese import is a key element of the OxyR response to hydrogen peroxide in *Escherichia coli*. *Mol. Microbiol. 72*, 844−858.
(11) Sobota, J. M., and Imlay, J. A. (2011) Iron enzyme ribulose-5-phosphate 3-epimerase in *Escherichia coli* is rapidly damaged by hydrogen peroxide but can be protected by manganese. *Proc. Natl. Acad. Sci. U.S.A. 108*, 5402−5407.
(12) Anjem, A., and Imlay, J. A. (2012) Mononuclear Iron Enzymes Are Primary Targets of Hydrogen Peroxide Stress. *J. Biol. Chem. 287*, 15544−15556.
(13) Archibald, F. S., and Fridovich, I. (1981) Manganese, superoxide dismutase, and oxygen tolerance in some lactic acid bacteria. *J. Bacteriol. 146*, 928−936.
(14) Daly, M. J., Gaidamakova, E. K., Matrosova, V. Y., Vasilenko, A., Zhai, M., Venkateswaran, A., Hess, M., Omelchenko, M. V., Kostandarithes, H. M., Makarova, K. S., Wackett, L. P., Fredrickson, J. K., and Ghosal, D. (2004) Accumulation of Mn(II) in *Deinococcus radiodurans* facilitates γ-radiation resistance. *Science 306*, 1025−1028.
(15) Daly, M. J., Gaidamakova, E. K., Matrosova, V. Y., Vasilenko, A., Zhai, M., Leapman, R. D., Lai, B., Ravel, B., Li, S. M., Kemner, K. M., and Fredrickson, J. K. (2007) Protein oxidation implicated as the primary determinant of bacterial radioresistance. *PLoS Biol. 5*, e92.
(16) Barnese, K., Gralla, E. B., Cabelli, D. E., and Valentine, J. S. (2008) Manganous phosphate acts as a superoxide dismutase. *J. Am. Chem. Soc. 130*, 4604−4606.
(17) Yesilkaya, H., Andisi, V. F., Andrew, P. W., and Bijlsma, J. J. E. (2013) *Streptococcus pneumoniae* and reactive oxygen species: An unusual approach to living with radicals. *Trends Microbiol. 21*, 187−195.
(18) Jacobsen, F. E., Kazmierczak, K. M., Lisher, J. P., Winkler, M. E., and Giedroc, D. P. (2011) Interplay between manganese and zinc homeostasis in the human pathogen *Streptococcus pneumoniae*. *Metallomics 3*, 38−41.
(19) McDevitt, C. A., Ogunniyi, A. D., Valkov, E., Lawrence, M. C., Kobe, B., McEwan, A. G., and Paton, J. C. (2011) A molecular mechanism for bacterial susceptibility to zinc. *PLoS Pathog. 7*, e1002357.
(20) Papp-Wallace, K. M., and Maguire, M. E. (2006) Manganese transport and the role of manganese in virulence. *Annu. Rev. Microbiol. 60*, 187−209.
(21) Lee, J. W., and Helmann, J. D. (2007) Functional specialization within the Fur family of metalloregulators. *BioMetals 20*, 485−499.
(22) D'Aquino, J. A., Tetenbaum-Novatt, J., White, A., Berkovitch, F., and Ringe, D. (2005) Mechanism of metal ion activation of the diphtheria toxin repressor DtxR. *Proc. Natl. Acad. Sci. U.S.A. 102*, 18408−18413.
(23) Ding, X., Zeng, H., Schiering, N., Ringe, D., and Murphy, J. R. (1996) Identification of the primary metal ion-activation sites of the diphtheria tox repressor by X-ray crystallography and site-directed mutational analysis. *Nat. Struct. Biol. 3*, 382−387.
(24) DeWitt, M. A., Kliegman, J. I., Helmann, J. D., Brennan, R. G., Farrens, D. L., and Glasfeld, A. (2007) The conformations of the manganese transport regulator of *Bacillus subtilis* in its metal-free state. *J. Mol. Biol. 365*, 1257−1265.
(25) Glasfeld, A., Guedon, E., Helmann, J. D., and Brennan, R. G. (2003) Structure of the manganese-bound manganese transport regulator of *Bacillus subtilis*. *Nat. Struct. Biol. 10*, 652−657.
(26) Golynskiy, M., Li, S., Woods, V. L., Jr., and Cohen, S. M. (2007) Conformational studies of the manganese transport regulator (MntR) from *Bacillus subtilis* using deuterium exchange mass spectrometry. *J. Biol. Inorg. Chem. 12*, 699−709.
(27) Golynskiy, M. V., Davis, T. C., Helmann, J. D., and Cohen, S. M. (2005) Metal-induced structural organization and stabilization of the metalloregulatory protein MntR. *Biochemistry 44*, 3380−3389.
(28) Golynskiy, M. V., Gunderson, W. A., Hendrich, M. P., and Cohen, S. M. (2006) Metal Binding Studies and EPR Spectroscopy of the Manganese Transport Regulator MntR. *Biochemistry 45*, 15359−15372.
(29) Lieser, S. A., Davis, T. C., Helmann, J. D., and Cohen, S. M. (2003) DNA-binding and oligomerization studies of the manganese(II) metalloregulatory protein MntR from *Bacillus subtilis*. *Biochemistry 42*, 12634−12642.
(30) Moore, C. M., Gaballa, A., Hui, M., Ye, R. W., and Helmann, J. D. (2005) Genetic and physiological responses of *Bacillus subtilis* to metal ion stress. *Mol. Microbiol. 57*, 27−40.
(31) Que, Q., and Helmann, J. D. (2000) Manganese homeostasis in *Bacillus subtilis* is regulated by MntR, a bifunctional regulator related to the diphtheria toxin repressor family of proteins. *Mol. Microbiol. 35*, 1454−1468.
(32) Kliegman, J. I., Griner, S. L., Helmann, J. D., Brennan, R. G., and Glasfeld, A. (2006) Structural basis for the metal-selective activation of the manganese transport regulator of *Bacillus subtilis*. *Biochemistry 45*, 3493−3505.
(33) McGuire, A. M., Cuthbert, B. J., Ma, Z., Grauer-Gray, K. D., Brunjes Brophy, M., Spear, K. A., Soonsanga, S., Kliegman, J. I., Griner, S. L., Helmann, J. D., and Glasfeld, A. (2013) Roles of the A and C sites in the manganese-specific activation of MntR. *Biochemistry 52*, 701−713.
(34) Stoll, K. E., Draper, W. E., Kliegman, J. I., Golynskiy, M. V., Brew-Appiah, R. A., Phillips, R. K., Brown, H. K., Breyer, W. A., Jakubovics, N. S., Jenkinson, H. F., Brennan, R. G., Cohen, S. M., and Glasfeld, A. (2009) Characterization and structure of the manganese-responsive transcriptional regulator ScaR. *Biochemistry 48*, 10308−10320.
(35) Pennella, M. A., Shokes, J. E., Cosper, N. J., Scott, R. A., and Giedroc, D. P. (2003) Structural elements of metal selectivity in metal sensor proteins. *Proc. Natl. Acad. Sci. U.S.A. 100*, 3713−3718.
(36) Reyes-Caballero, H., Guerra, A. J., Jacobsen, F. E., Kazmierczak, K. M., Cowart, D., Koppolu, U. M., Scott, R. A., Winkler, M. E., and Giedroc, D. P. (2010) The metalloregulatory zinc site in *Streptococcus pneumoniae* AdcR, a zinc-activated MarR family repressor. *J. Mol. Biol. 403*, 197−216.
(37) Grossoehme, N. E., and Giedroc, D. P. (2012) Illuminating allostery in metal sensing transcriptional regulators. *Methods Mol. Biol. 875*, 165−192.
(38) Hanlon, D. P., Watt, D. S., and Westhead, E. W. (1966) The interaction of divalent metal ions with tris buffer in dilute solution. *Anal. Biochem. 16*, 225−233.
(39) Kuzmic, P. (1996) Program DYNAFIT for the analysis of enzyme kinetic data: Application to HIV proteinase. *Anal. Biochem. 237*, 260−273.
(40) Campanello, G. C., Ma, Z., Grossoehme, N. E., Guerra, A. J., Ward, B. P., DiMarchi, R. D., Ye, Y., Dann, C. E., III, and Giedroc, D. P. (2013) Allosteric Inhibition of a Zinc-Sensing Transcriptional Repressor: Insights into the Arsenic Repressor (ArsR) Family. *J. Mol. Biol. 425*, 1143−1157.
(41) Leitch, S., Bradley, M. J., Rowe, J. L., Chivers, P. T., and Maroney, M. J. (2007) Nickel-specific response in the transcriptional regulator *Escherichia coli* NikR. *J. Am. Chem. Soc. 129*, 5085−5095.
(42) Padden, K. M., Krebs, J. F., MacBeth, C. E., Scarrow, R. C., and Borovik, A. S. (2001) Immobilized metal complexes in porous organic hosts: Development of a material for the selective and reversible binding of nitric oxide. *J. Am. Chem. Soc. 123*, 1072−1079.

(43) Webb, S. M. (2005) SIXpack: A graphical user interface for XAS analysis using IFEFFIT. *Phys. Scr. T115*, 1011−1014.
(44) Ankudinov, A. L., Ravel, B., Rehr, J. J., and Conradson, S. D. (1998) Real-space multiple-scattering calculation and interpretation of X-ray-absorption near-edge structure. *Phys. Rev. B 58*, 7565−7576.
(45) Zabinsky, S. I., Rehr, J. J., Ankudinov, A., Albers, R. C., and Eller, M. J. (1995) Multiple-scattering calculations of X-ray-absorption spectra. *Phys. Rev. B: Condens. Matter Mater. Phys. 52*, 2995−3009.
(46) Gasper, R., Scrima, A., and Wittinghofer, A. (2006) Structural insights into HypB, a GTP-binding protein that regulates metal binding. *J. Biol. Chem. 281*, 27492−27502.
(47) Costello, A. L., Sharma, N. P., Yang, K. W., Crowder, M. W., and Tierney, D. L. (2006) X-ray absorption spectroscopy of the zinc-binding sites in the class B2 metallo-β-lactamase ImiS from *Aeromonas veronii* bv. sobria. *Biochemistry 45*, 13650−13658.
(48) Costello, A., Periyannan, G., Yang, K. W., Crowder, M. W., and Tierney, D. L. (2006) Site-selective binding of Zn(II) to metallo-β-lactamase L1 from *Stenotrophomonas maltophilia*. *J. Biol. Inorg. Chem. 11*, 351−358.
(49) Herbst, R. W., Guce, A., Bryngelson, P. A., Higgins, K. A., Ryan, K. C., Cabelli, D. E., Garman, S. C., and Maroney, M. J. (2009) Role of conserved tyrosine residues in NiSOD catalysis: A case of convergent evolution. *Biochemistry 48*, 3354−3369.
(50) Jacquamet, L., Aberdam, D., Adrait, A., Hazemann, J. L., Latour, J. M., and Michaud-Soret, I. (1998) X-ray absorption spectroscopy of a new zinc site in the fur protein from *Escherichia coli*. *Biochemistry 37*, 2564−2571.
(51) Ma, Z., Faulkner, M. J., and Helmann, J. D. (2012) Origins of specificity and cross-talk in metal ion sensing by *Bacillus subtilis* Fur. *Mol. Microbiol. 86*, 1144−1155.
(52) Reyes-Caballero, H., Campanello, G. C., and Giedroc, D. P. (2011) Metalloregulatory proteins: Metal selectivity and allosteric switching. *Biophys. Chem. 156*, 103−114.
(53) Yesilkaya, H., Kadioglu, A., Gingles, N., Alexander, J. E., Mitchell, T. J., and Andrew, P. W. (2000) Role of manganese-containing superoxide dismutase in oxidative stress and virulence of *Streptococcus pneumoniae*. *Infect. Immun. 68*, 2819−2826.
(54) Jiang, Y.-L., Zhang, J.-W., Yu, W.-L., Cheng, W., Zhang, C.-C., Frolet, C., Di Guilmi, A.-M., Vernet, T., Zhou, C.-Z., and Chen, Y. (2011) Structural and Enzymatic Characterization of the Streptococcal ATP/Diadenosine Polyphosphate and Phosphodiester Hydrolase Spr1479/SapH. *J. Biol. Chem. 286*, 35906−35914.
(55) Morona, J. K., Morona, R., Miller, D. C., and Paton, J. C. (2002) *Streptococcus pneumoniae* capsule biosynthesis protein CpsB is a novel manganese-dependent phosphotyrosine-protein phosphatase. *J. Bacteriol. 184*, 577−583.
(56) Kloosterman, T. G., Witwicki, R. M., van der Kooi-Pol, M. M., Bijlsma, J. J., and Kuipers, O. P. (2008) Opposite effects of Mn^{2+} and Zn^{2+} on PsaR-mediated expression of the virulence genes *pcpA, prtA,* and *psaBCA* of *Streptococcus pneumoniae*. *J. Bacteriol. 190*, 5382−5393.
(57) Guedon, E., and Helmann, J. D. (2003) Origins of metal ion selectivity in the DtxR/MntR family of metalloregulators. *Mol. Microbiol. 48*, 495−506.
(58) White, A., Ding, X., vanderSpek, J. C., Murphy, J. R., and Ringe, D. (1998) Structure of the metal-ion-activated diphtheria toxin repressor/tox operator complex. *Nature 394*, 502−506.
(59) Golynskiy, M., Li, S., Woods, V. L., Jr., and Cohen, S. M. (2007) Conformational studies of the manganese transport regulator (MntR) from *Bacillus subtilis* using deuterium exchange mass spectrometry. *JBIC, J. Biol. Inorg. Chem. 12*, 699.
(60) Pohl, E., Holmes, R. K., and Hol, W. G. (1999) Crystal structure of a cobalt-activated diphtheria toxin repressor-DNA complex reveals a metal-binding SH3-like domain. *J. Mol. Biol. 292*, 653−667.
(61) Pohl, E., Holmes, R. K., and Hol, W. G. (1999) Crystal structure of the iron-dependent regulator (IdeR) from *Mycobacterium tuberculosis* shows both metal binding sites fully occupied. *J. Mol. Biol. 285*, 1145−1156.
(62) Changela, A., Chen, K., Xue, Y., Holschen, J., Outten, C. E., O'Halloran, T. V., and Mondragon, A. (2003) Molecular basis of metal-ion selectivity and zeptomolar sensitivity by CueR. *Science 301*, 1383−1387.
(63) Pennella, M. A., Arunkumar, A. I., and Giedroc, D. P. (2006) Individual metal ligands play distinct functional roles in the zinc sensor *Staphylococcus aureus* CzrA. *J. Mol. Biol. 356*, 1124−1136.
(64) Ma, Z., Cowart, D. M., Ward, B. P., Arnold, R. J., DiMarchi, R. D., Zhang, L., George, G. N., Scott, R. A., and Giedroc, D. P. (2009) Unnatural amino acid substitution as a probe of the allosteric coupling pathway in a mycobacterial Cu(I) sensor. *J. Am. Chem. Soc. 131*, 18044−18045.
(65) Ma, Z., Cowart, D. M., Scott, R. A., and Giedroc, D. P. (2009) Molecular insights into the metal selectivity of the copper(I)-sensing repressor CsoR from *Bacillus subtilis*. *Biochemistry 48*, 3325−3334.
(66) Lee, C. W., Chakravorty, D. K., Chang, F. M., Reyes-Caballero, H., Ye, Y., Merz, K. M., Jr., and Giedroc, D. P. (2012) Solution structure of *Mycobacterium tuberculosis* NmtR in the apo state: Insights into Ni(II)-mediated allostery. *Biochemistry 51*, 2619−2629.
(67) Trepreau, J., Girard, E., Maillard, A. P., de Rosny, E., Petit-Haertlein, I., Kahn, R., and Coves, J. (2011) Structural basis for metal sensing by CnrX. *J. Mol. Biol. 408*, 766−779.
(68) Foster, A. W., Patterson, C. J., Pernil, R., Hess, C. R., and Robinson, N. J. (2012) Cytosolic Ni(II) sensor in cyanobacterium: Nickel detection follows nickel affinity across four families of metal sensors. *J. Biol. Chem. 287*, 12142−12151.
(69) Waldron, K. J., and Robinson, N. J. (2009) How do bacterial cells ensure that metalloproteins get the correct metal? *Nat. Rev. Microbiol. 7*, 25−35.
(70) Ma, Z., Lee, J. W., and Helmann, J. D. (2011) Identification of altered function alleles that affect *Bacillus subtilis* PerR metal ion selectivity. *Nucleic Acids Res. 39*, 5036−5044.
(71) Hayden, J. A., Brophy, M. B., Cunden, L. S., and Nolan, E. M. (2013) High-affinity manganese coordination by human calprotectin is calcium-dependent and requires the histidine-rich site formed at the dimer interface. *J. Am. Chem. Soc. 135*, 775−787.
(72) Puri, S., Hohle, T. H., and O'Brian, M. R. (2010) Control of bacterial iron homeostasis by manganese. *Proc. Natl. Acad. Sci. U.S.A. 107*, 10691−10695.